A machine learning based optimisation method to evaluate the crushing behaviours of square tubes with rectangular-hole-type initiators

Liang, R., Xu, F., Liu, N., Liu, X., Bastien, C. & Zhang, C

Original citation & hyperlink:
Liang, R, Xu, F, Liu, N, Liu, X, Bastien, C & Zhang, C 2024, 'A machine learning based optimisation method to evaluate the crushing behaviours of square tubes with rectangular-hole-type initiators', International Journal of Crashworthiness, vol. 29, no. 1, pp. 115-131. https://doi.org/10.1080/13588265.2023.2189000

DOI 10.1080/13588265.2023.2189000
ISSN 1358-8265
ESSN 1754-2111

Publisher: Taylor and Francis

A machine learning based optimization method to evaluate the crushing behaviors of square tubes with rectangular-hole-type initiators

Rui Liang[1], Fengxiang Xu[2, 3], Na Liu[1 *], Xiang Liu[1], Christophe Bastien[4], Cheng Zhang[1]

1. School of Automobile Engineering, Guilin University of Aerospace Technology, Guilin 400054, China;
2. Hubei Key Laboratory of Advanced Technology of Automotive Components, Wuhan University of Technology, Wuhan 430070, China;
3. Hubei Collaborative Innovation Center for Automotive Components Technology, Wuhan University of Technology, Wuhan 430070, China;
4. Centre of Future Transport and Cities, Coventry University, Coventry CV1 2TE, UK

Abstract: Rectangular-hole-type crush initiators have attracted much attention due to their exceptional advantages in improving crashworthiness performance. Unfortunately, undesired deformation buckling modes i.e., bifurcation buckling, can occur and challenge optimization processes. This paper aims remedies to this limitation and proposes a machine learning based optimization method that removes these undesired deformation modes to effectively evaluate the effect of initiators' parameters in improving crush response. First, finite element models of square tubes with different numbers and positions of initiators were built and computed. Second, the complex proportional assessment (COPRAS) method was adopted to rank the crashworthiness characteristics. The results demonstrated that square tubes with two sets of four corner holes along the axial direction were the best choice. Finally, the optimization method based on machine learning was employed to evaluate the influence of the initiator's size on the crushing behaviors for minimizing the initial peak force (IPF), maximizing the energy absorption (EA), and crushing force efficiency (CFE). The results illustrated that the IPF of the optimized design Pareto front upper limit is about 21.94% lower, with 0.08% and 36.67% higher EA and CFE, respectively, than those of the best choice observed from COPRAS. This study highlights the ability of the proposed machine learning based optimization method to improve crashworthiness performance.

Keywords: Machine learning; Rectangular-type crush initiator; Crashworthiness performance; Deformation mode

*Corresponding Author: Email: naliu1989@126.com (Na Liu)

Formatted: French (France)

1. Introduction

Thin-walled square tube structures have been widely applied in vehicles as energy absorbers to protect passengers from severe injury due to their excellent energy absorption and resistance to deformation [1]. The square tubes are expected to fold as progressive buckling to absorb more impact energy during an impact [2]. However, square tubes usually collapse in Eulerian buckling mode with a high peak load and lower energy absorption [3]. Hence, much effort has been devoted to understanding and improving the thin-walled square tube structures' crashworthiness performance.

Over the past decades, many significant research achievements have been made [4]. Additionally, initiators were identified as the most significant influencing factors resulting in the square tube being folded conventionally to achieve a lower peak impact force and improved energy absorption [5-7].

Furthermore, different initiator configurations have been proposed, including dent-type initiators, rib-type initiators, hole-type initiators, and rectangular-type initiators [8-12]. For instance, Mamalis et al. [12] investigated the influence of crush initiators' position on crashworthiness performance. In their research, the square tube began to deform from the position of the initiators during the impact. Moreover, the initial peak force of a square tube with initiators near the top decreased by 2.13% and 0.58%, respectively, than the without initiators case and the initiators in the middle case. Along with the position, the initiators' depth also plays an essential role in controlling the quality and the quantity of thin-walled tubes' energy absorption [6].

Through different experiments, Cho et al. [13] further investigated the impact of the rib-dent-type initiators' depth and width on crashworthiness performance. Their results demonstrated that the large dent depth of the crush initiator showed a much higher impact force. Furthermore, Yamaguchi et al.[5] proposed to investigate the effects of various beading shapes and pitches. In their research, corner beading and web beading were investigated. Their results illustrated that the corner beading reduced the force by 20% compared to beading.

On the other hand, failure induced by the hole-type initiators might be another effective tunable parameter on crushable components. Eren et al. [2] studied the axial

crushing behavior of square tubes with dent-type initiators, rib-type initiators, and hole-type initiators. Their results demonstrated that the hole-type initiator with suitable size parameters might have similar crashworthiness performance as dent-type and rib-type initiators. Besides, in the applications of engineering structure, the hole-type initiators were adopted as the preferred initiators to reduce the initial peak force and maintain progressive crushing during the impact with the benefit of lightweight [14].

Consequently, much research has been proposed to study the hole-type square tubes' crashworthiness mechanics. Typically, the effective influence of circle-hole-type initiators was further conducted by Tarlochan et al.[15]. Their experimental and numerical results suggested that the peak force could be decreased from 316 kN to 284 kN with a 7% crush force efficiency increase. Nia et al. [16] proposed to improve the square tubes' energy absorption by employing diamond-hole-type initiators. Their results showed that the mean crushing force could be improved to 50.77%.

Cheng et al. [10] suggested studying the hole-type initiator's thin-walled square tube's crashworthiness by changing the size of the initiators. In their research, twenty specimens were employed to investigate the influence of the initiator's size on the crashworthiness performance. Their results show that the initial peak force (IPF) decreases as the size increases. A 13.49% IPF decrease could be found when the hole size changed from 7.14 mm to 14.29 mm. Han et al. [17] further investigated the effectiveness of the hole-type initiators' location on the crashworthiness performance. His research provided diamond, circular, and rectangular holes in the middle surface and the corner of the square tubes. Those results indicated that tubes with rectangular-hole-type initiators perform better crashworthiness performance.

Bodlani et al. [18] researched the effect of hole count on crashworthiness performance. The number of perforations spaced throughout the tube length varied between two and ten in their investigation. Their results indicated that increasing the number of holes beyond two does not result in a further significant reduction in the initial peak force. The discoveries of rectangular-hole-type initiators could effectively induce failure modes and further improve crashworthiness. Two rectangular-hole-type initiators provided a favorable crashworthiness characteristic. Machine learning

technology has an excellent processing ability for complex parameters, making it applied to the research of crashworthiness analysis [19-21].

However, few of the research papers mentioned above focus on deformation mode [22]. Besides, the results of the deformation mode prediction is a discrete value, not an approximate prediction of a constant value. Nevertheless, traditional data fitting methods obtain continuous polynomial functions. Thus, traditional data fitting methods are challenging to find the influence of the parameters of the structure fittings on the deformation mode.

Fortunately, artificial intelligence technology, especially the classification algorithm of machine learning technology, makes it easy to analyze the influence of initiator parameters on the deformation mode. Li et al. [22] used machine learning, including K-nearest neighbor, support vector machine, and random forest, to remove the undesired deformation of thin-walled shrink tubes. However, ~~to the best of the authors' knowledge,~~ the influence of initiator parameters on the crashworthiness performance and optimal crashworthiness performance by considering the initiator parameters and the deformation mode has not been widely investigated and reported.

This paper proposes a machine learning based optimization method to remove the undesired deformation mode and investigate the influence of the initiator' parameter on the crashworthiness, resulting in an optimized energy-absorbing square tube with the initiator. The mechanical behavior of IPF, EA, CFE, and deformation mode is adopted as criteria to assess its crashworthiness performance. It is the first study using machine learning to remove undesired deformations and further study the impact of hole-type initiator's parameters on crashworthiness.

2 Methods and Materials

2.1 Machine learning

The machine learning method, including K-nearest neighbor (KNN), support vector machine (SVM), and random forest (RF) that can perform classification and regression, were used to remove undesired deformations, predicting the effect of the hole-type crush initiator on crashworthiness performance.

The KNN algorithm measures the distance between different eigenvalues for classification [23, 24]. When inputting the new data to be predicted, KNN compares each feature of the new data with the features corresponding to the data in the training sample set and then extracts the category with the most occurrences amongst the k most similar data (nearest neighbors) in the feature set as the new data [23].

The basic idea of SVM is to find an optimal hyperplane to maximize the classification gap [25]. In predicting, the SVM algorithm for classification and regression finds a plane in the space that can effectively separate the two samples based on the existing sample points and their output values [26].

RF, which could also be employed for classification and regression prediction, is a method to construct tree-based classifiers whose capacity can be arbitrarily expanded for increases in accuracy for both training and unseen data [27, 28].

2.2 Finite element modeling

To further investigate and verify the machine learning based optimization proposed in this study, nonlinear finite element code LS-Dyna was employed to built up finite element (FE) models of square tubes. The dynamic axial impact experiment setup by Langseth et al. [29] was used to varify the FE models. Their test rig is presented in Fig 1.(a), in which the tube was clamped by the clamping device and the cover was impact by the impactor device. Fig.1 (b) and (c) demonstrated the geometrical configuration of the square tube considered in this study. A 56 kg impactor with an initial velocity of 15 m/s hit the square tube's upper side, while a clamper restrained all directions of the lower square tube, as shown in Fig.4. The static and dynamic friction coefficients between the inner, the outer square tube and the clamper were 0.4 [30]. Accordting to previous research [31], the Belytschklo-Lin-Tsay thin-shell elements were utilized to simulate the impactor, the tube wall and the clamping device. The element sizes of tube and clamper were set as 2×2 mm^2, while the that of the impactor was asjusted as 10×10 mm^2 to balance the accuracy of the simulation and the computational cost. Based on previous research [29], ~~T~~the 24 material model was employed to model the AA6060 T4 material–[29]. Table 1 and Fig. 2 illustrate the material constants. Furthermore, the

aluminum alloy material is insensitively of strain rate [32, 33]. Hence, the effect of straion rete in this model is neglected.

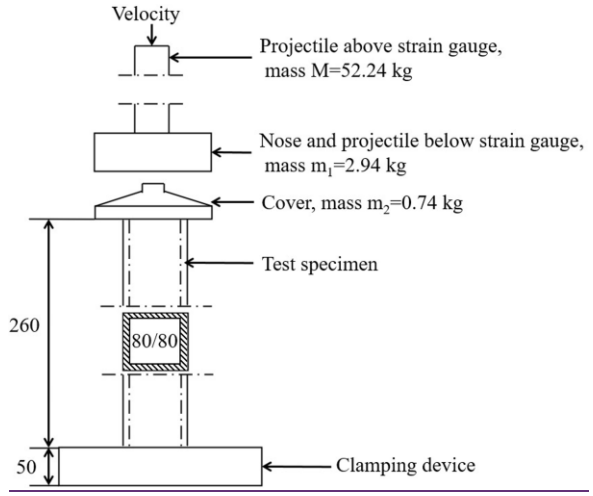

(a) Section of test rig

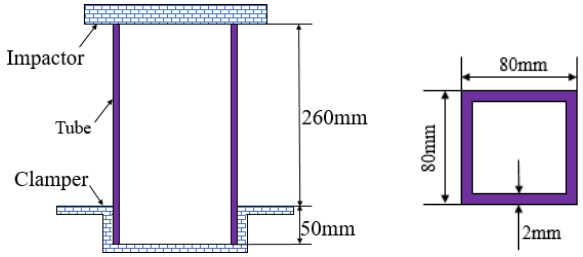

(~~a~~b) Front view (~~b~~c) Top view

Fig. 1 Section of test rig and ~~G~~the geometrical configuration of the square tube ~~and its impact condition~~.

Table 1 The mechanical properties of the AA6060 T4 [29]

Density	Young's modulus	Initial yield stress	Ultimate stress	Poisson's ratio	Power law exponent
2.7×10^3kg/m^3	68.2 GPa	80 MPa	173 MPa	0.3	0.23

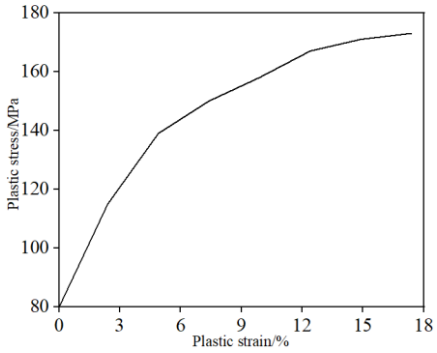

Fig. 2 Plastic stress versus plastic strain of AA6060 T4 [29].

2.3 Crashworthiness indicators

The initial peak force (IPF), energy absorption (EA), and crush force efficiency (CFE) are the most commonly adopted crashworthiness indicators to evaluate the energy absorbing structures' crashworthiness [34, 35]. Based on previous research [36], the IPF, EA, and CFE were defined as follow:

The EA can be expressed as:

$$\mathrm{EA}(d) = \int_0^d F(x)dx \qquad (1)$$

Where d is crushing distance, F(x) denotes the instantaneous crushing force at displacement x.

The CFE can be defined by:

$$\mathrm{CFE} = \frac{MCF(d)}{\mathrm{IPF}} \qquad (2)$$

Where IPF denotes the first peak value of F(x) in the early stage, MCF(d) is the mean crushing force, which is calculated mathematically as:

$$\mathrm{MCF(d)} = \frac{EA(d)}{d} \qquad (3)$$

Note that the higher the CFE, the more efficient the structure, and CFE was calculated at the maximum compressed displacement ($d_{max.}$).

2.4 Validation of the finite element model

The square tube finite element model will be constructed and validated based on previous researches [29]. The comparison between the experimental and finite element numerical results was graphed in Fig. 3 and 4. The results demonstrated that the errors of the IPF and EA between numerical and experiment is 0.7% and 1.6% respectively.

In addition, the simulation's force versus displacement curves could capture the experiment's true bucking behaviors. Fig. 5 illustrates that both the simulation and experiment model demonstrated two folds and a slight right tilt during the impact, indicating that the simulations agreed well with those of the experiments, confirming the model validation.

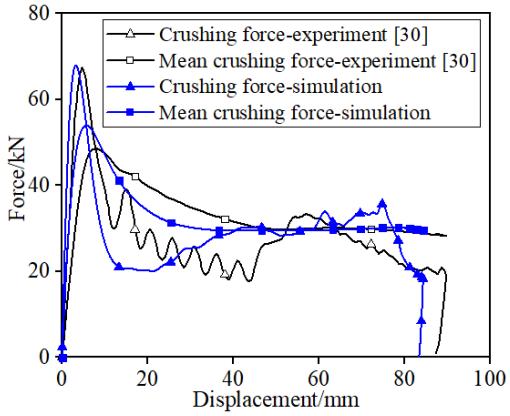

Fig. 3 Force versus displacement of the AA 6060 T4 square tubes.

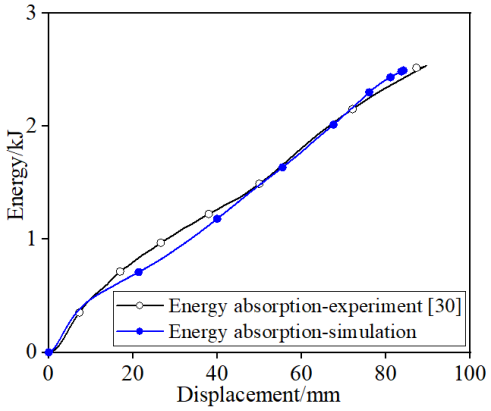

Fig. 4 Energy absorption versus displacement of the AA 6060 T4 square tubes.

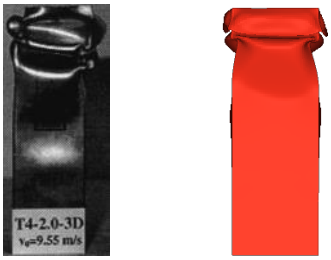

(a) Experiment [29] (b) Simulation

Fig. 5 Deformation mode of the AA 6060 T4 square tubes.

2.5 The framework of the machine learning optimization method

Traditional discrete or continuous optimization algorithms have a huge computational cost in the case of little-known domain information, especially for mixed regression and classification problems [22, 37]. The machine learning optimization method proposed to optimize the square tube' crashworthiness performance consists of three phases, as illustrated in Fig.6: Phase I data collection, Phase II machine learning, and Phase III optimization.

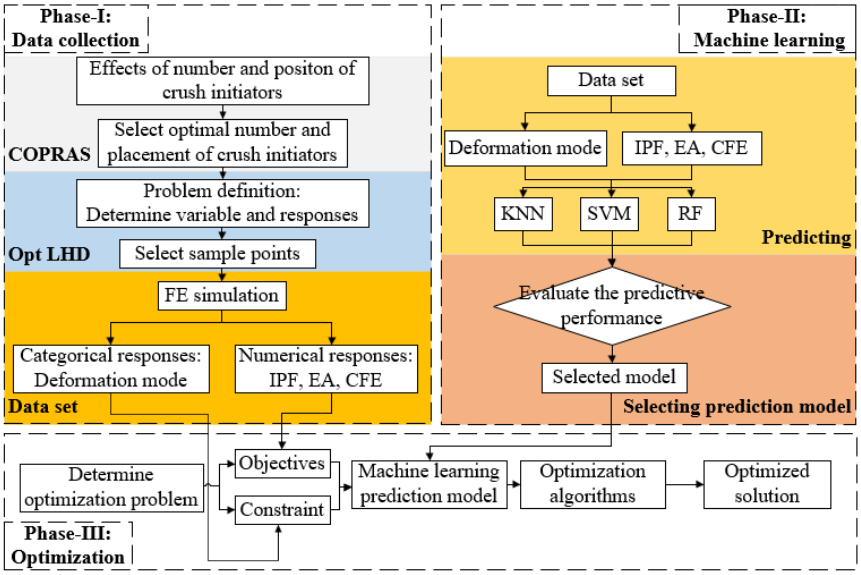

Fig.6 The flow chart of the machine learning optimization method

In the Data Collection Phrase, the first step was selected the competitive number and location of initiators using a complex proportional assessment (COPRAS) method, hence selecting the most appropriate design variables. Then, the optimal Latin hypercube design was used to populate a design space with 150 design variable permutations. The crashworthiness performance of the square tube was examined by analyzing the deformation mode, IPF, EA, and CFE from a finite-element simulation.

In Phase II, all the crush response are described as single-objective problems with continuous optimization using machine learning. The critical role of this Phase is to achieve samples uniformly in the sampling space and obtain a reliable predictive model.

In Phase III, machine learning that showed the best prediction performance in Phase II minimizes IPF and maximizes EA and CFE, considering the deformation mode.

3 Effects of number and placement of crush initiators

Evidence has shown that the collapse begins at the initiators' location [14]. Besides, no more than two initiators in the axial direction of the corners result in a better crashworthiness performance than the other configurations [2, 18]. Thus, to study the effects of the different number of initiators, several square tubes with initiators were conducted, as shown in Fig. 7 (b)-10(e). Different designs were conceived for four different numbers of initiators along a radial direction, including one corner hole (Model A-15), a set of two corner holes (Model B-15), a set of three corner holes (Model C-15), and a set of four-corner-holes (Model D-15). Additional designs with two sets of initiators along a radial direction were also conducted to study the effect of the number and placement of initiators on the energy absorption characteristics and deformation modes of the square tubes, as shown in Fig. 7 (f)-10(i).

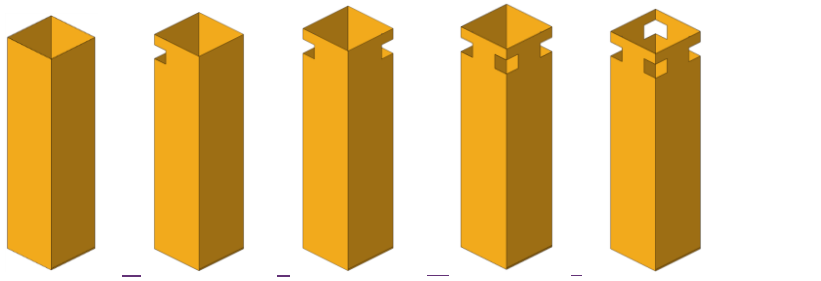

(a) Baseline (b) Model A-15 (c) Model B-15 (d) Model C-15 (e) Model D-15

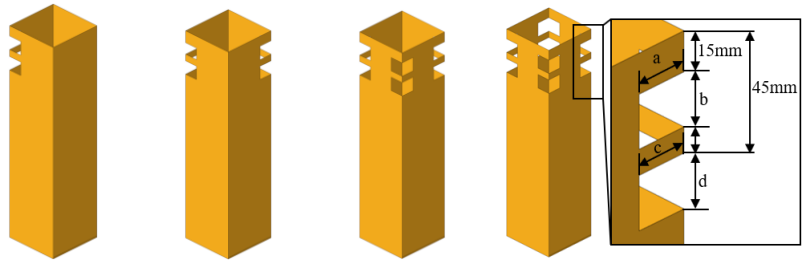

(f) Model A-15-45 (g) Model B-15-45 (h) Model C-15-45 (i) Model D-15-45

Fig. 7 Square tubes with one and two rectangular-hole-type initiators along the axial direction.

All the specimens were marked as Model X-N_1-N_2 herein, in which X denotes the number of initiators, while N_1 and N_2 denote the distance of the first and second initiator

from the top surface of the square tube. For instance, Model D-15-45 denotes specimen (D) with four initiators along a radial direction, and the first set of initiators located at a distance of 15 mm from the top surface of the square tube, while the distance of the second set of initiator was 45 mm, as shown in Fig 7 (i).

3.1 Effects of the number and position of crush initiators along radial direction

Aside from the number of hole-type initiators in the radial direction, the number of induced holes in the axial direction and their locations also significantly affect the crashworthiness performance [18]. The influence of the crush initiator' number along the radial direction on deformation mode is presented in Table 2.

Table 2 Deformation modes of tubes.

Model A-15	Model B-15	Model C-15	Model D-15
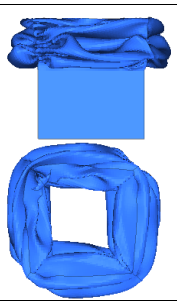			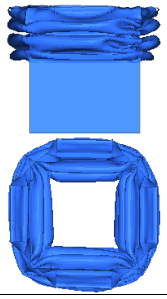
Model A-15-45	**Model B-15-45**	**Model C-15-45**	**Model D-15-45**
		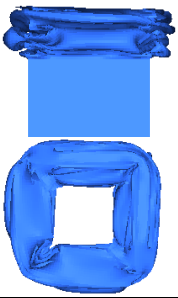	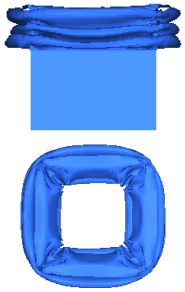

The square tubes with four corner holes exhibit a combination of a symmetrical compression-type deformation because of the section's symmetry property, as reported in Ref. [25, 38]. The other square tubes exhibit non-centrosymmetric deformation modes. In the same crush initiator' number along radial direction situation, tubes with two sets of initiators along the axial direction exhibit greater axial compression than

those of tubes with one set of initiators, most notably evidenced by the more significant axial deformation of Model D-15-45 than Model D-15.

Fig. 8 graphed the crush responses of the square tubes in terms of IPF, EA, and CFE. The results illustrate that additional initiators reduce the IPF compared to those of the baseline, with a notable increase in ~~EA and~~ CFE. In addtion, adding a initiators could improve the energy absorption of the square tubes. However, the square tubes with different number of initiators present almost the same energy absorption value. Besides, Model D-15 and Model A-15-45 demonstrate a lower IPF than others. Moreover, an additional number of initiators along the axial direction yields higher CFE, while an additional number of initiators along the radial direction shows a comparable increase in CFE. Fig. 8 suggests that the crush responses can be enhanced by selecting the appropriate number of initiators.

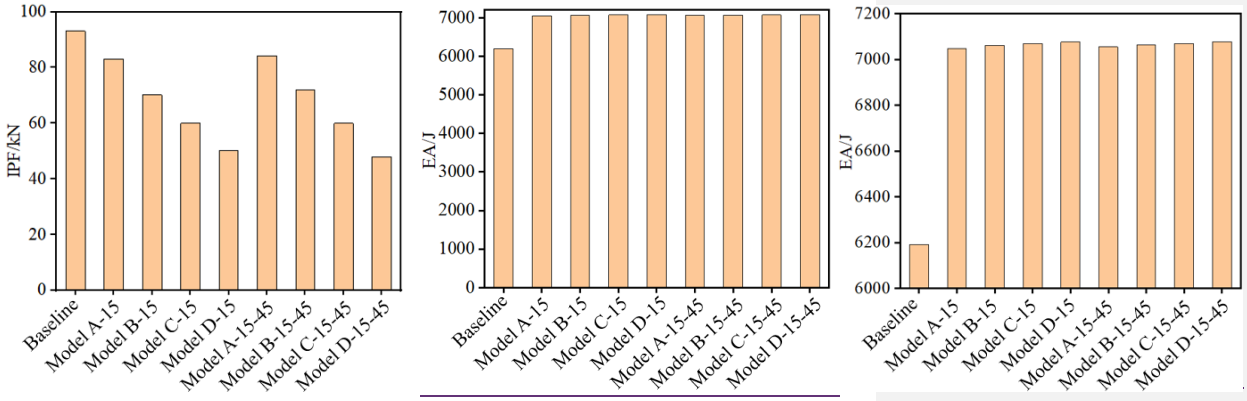

(a) (b)

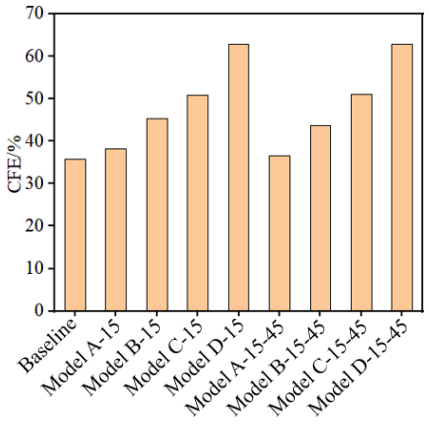

(c)

Fig. 8 Effects of initiator' number on (a) IPF; (b) EA; (c) CFE.

3.2 Effects of position of crush initiators along the radial direction

The influence degree differs for different numbers and positions of initiators, making it challenging to illustrate the optimal number and position of the initiators. COPRAS method was thus adopted herein to rank initiator crashworthiness performance. The steps of COPRAS method are divided into the following seven steps [39-41]:

Step 1: Define the initial decision matrix X.

$$X = \left[x_{ij} \right]_{mn} = \begin{bmatrix} x_{11} & x_{12} & \cdots & x_{1j} \\ x_{21} & x_{22} & \cdots & x_{2j} \\ \cdots & \cdots & \cdots & \cdots \\ x_{m1} & x_{m2} & \cdots & x_{mn} \end{bmatrix} \tag{4}$$

where x_{ij} is the performance value of the i-th alternative on the j-th criteria, m is the number of design alternatives, and n is the number of criteria.

Step 2: Determine the nondimensionalized matrix R.

A nondimensionalized matrix R that could be used to overcome most design criteria is not the same dimensions or unit, which was proposed to convert the entire matrix X.

$$R = \left[r_{ij} \right] = \frac{x_{ij}}{\sum_{i=1}^{m} x_{ij}} \tag{5}$$

where the entry x_{ij} is the absolute value for each criterion, $\sum x_{ij}$ represents the summation for several positive decisions.

Step 3: Fix the weighted normalized decision matrix D.

$$D = \left[y_{ij} \right] = r_{ij} \times w_j \tag{6}$$

where the r_{ij} represents the normalized performance value of the i-th alternative on the j-th criterion, and w-j is the j-th criterion's weight. $\sum_{k=1}^{j} w_j = 1$.

Step 4：Define the weighted w_j.

The w_j could be defined as:

$$w_j = \frac{W_j}{G} \tag{7}$$

The total score of all criteria could be defined as:

$$G = \sum_{i=1}^{m} W_j \tag{8}$$

where toral comparison sets (N) are equal to N=(n(n-1)/2) in which n is the number of selection criteria.

In this paper, the SEA and CFE were given a higher weighting than the IPF, as shown in Table 3.

Table 3. Weightage setting for each performance indicator

Selection criteria	Number of comparison sets, N=3(3-1)/2=3			W_j	w_j
	1	2	3		
IPF	2	3		5	5/12=0.42
EA	2		3	5	5/12=0.42
CFE		1	1	2	2/12=0.17
				12	1

The criterion for determining the weight W_j of j-th could be described as:

$$W_j = \sum_{i=1}^{m} N_{ij} \tag{9}$$

Step 5：Sum the weighted of beneficial and non-beneficial attributes.

$$S_{+} = \sum_{i=1}^{m} S_{+i} = \sum_{i=1}^{m} \sum_{j=1}^{n} y_{+ij} \tag{10}$$

$$S_{-} = \sum_{i=1}^{m} S_{-i} = \sum_{i=1}^{m} \sum_{j=1}^{n} y_{-ij} \tag{11}$$

$$S_{-\min} = \min S_{-i} \tag{12}$$

where the y_{+ij} and y_{-ij} represent the beneficial and non-beneficial attributes, respectively. S_{-min} is the minimal value of S_{-i}. The greater S_{+i} together with the lower S_{-i}, the better is the design concept.

The EA and CFE were calculated as beneficial attributes, while the IPF was adopted as a non-beneficial attribute [42].

Step 6：Relative significance or priority Q_i.

$$Q_i = S_{+i} + \frac{S_{-\min}\sum_{i=1}^{m} S_{-i}}{S_{-i}\sum_{i=1}^{m}(S_{-\min}/S_{-i})} \tag{13}$$

A higher value of Q_i indicates a better design case.

Step 7：Calculate the quantitative utility U_i for the i-th alternative.

$$U_i = \frac{Q_i}{Q_{\max}} \times 100\% \tag{14}$$

Where the Q_{max} is the maximum value of the relative significance or priority.

The crashworthiness responses, Q_i and quantitative utility U_i were listed in Table 4. A higher value of U_i indicates a better crashworthiness performance[42]. Thus, the Model D-15-45 was the best choice, due to it induces a lower IPF and a higher EA.

Table 4 Effect of position of initiator on the square tube crashworthiness performance

Models	IPF/kN	EA/J	CFE/%	Q_i	U_i	Rank
Baseline	93.11	6190.92	35.72	0.01339	64.36521	61
Model A-15	83.17	7054.57	38.28	0.01500	72.13145	41
Model A-45	83.84	7048.10	37.83	0.01492	71.74242	44
Model A-75	87.22	7046.95	35.54	0.01456	69.98998	52
Model A-105	89.83	7047.97	34.78	0.01435	68.99801	57
Model A-135	92.56	7049.18	34.83	0.01420	68.25453	60
Model A-15-45	84.17	7054.78	36.61	0.01483	71.30900	49
Model A-15-75	84.82	7055.30	37.67	0.01485	71.41301	46
Model A-15-105	84.42	7055.11	37.17	0.01485	71.39199	48
Model A-15-135	89.93	7054.75	33.95	0.01430	68.75397	59
Model A-45-75	84.12	7048.16	36.38	0.01481	71.22403	50
Model A-45-105	84.14	7048.50	38.27	0.01493	71.77589	42
Model A-45-135	84.07	7048.38	37.42	0.01488	71.55011	45
Model A-75-105	87.14	7046.96	35.33	0.01455	69.95262	53
Model A-75-135	87.00	7046.79	34.81	0.01453	69.84086	55
Model A-105-135	89.68	7047.87	34.45	0.01434	68.94247	58
Model B-15	70.23	7061.36	45.38	0.01652	79.40270	22
Model B-45	72.36	7046.97	44.65	0.01625	78.14583	25
Model B-75	79.25	7044.03	41.19	0.01546	74.31843	36
Model B-105	84.96	7045.63	38.59	0.01489	71.59369	43
Model B-135	90.32	7048.08	36.21	0.01441	69.28043	54
Model B-15-45	71.97	7062.56	43.70	0.01625	78.10918	26
Model B-15-75	72.73	7062.93	43.49	0.01616	77.71516	31
Model B-15-105	71.99	7062.67	46.78	0.01643	79.01202	23
Model B-15-135	71.30	7062.19	37.73	0.01484	71.34999	47
Model B-45-75	72.46	7046.82	44.03	0.01633	78.50969	24
Model B-45-105	72.49	7047.20	41.10	0.01603	77.05424	33
Model B-45-135	72.33	7047.04	44.13	0.01621	77.93440	29
Model B-75-105	79.00	7043.88	42.95	0.01615	77.66064	32
Model B-75-135	78.86	7043.81	39.27	0.01536	73.84949	38
Model B-105-135	84.92	7045.57	40.64	0.01546	74.30401	37
Model C-15	60.00	7068.94	50.89	0.01803	86.69917	11
Model C-45	64.08	7047.12	49.93	0.01744	83.85395	17

Model C-75	72.48	7041.22	43.84	0.01619	77.82794	30
Model C-105	81.07	7043.15	37.86	0.01512	72.67702	40
Model C-135	88.27	7046.65	35.33	0.01448	69.61248	56
Model C-15-45	59.93	7070.15	51.05	0.01805	86.79914	10
Model C-15-75	61.52	7070.64	50.47	0.01781	85.62722	14
Model C-15-105	60.90	7069.94	50.24	0.01788	85.94022	13
Model C-15-135	60.51	7069.56	49.59	0.01789	85.99180	12
Model C-45-75	62.78	7046.66	48.12	0.01749	84.06487	16
Model C-45-105	63.86	7047.48	47.98	0.01735	83.40378	19
Model C-45-135	63.97	7047.37	49.50	0.01743	83.78618	18
Model C-75-105	71.13	7040.33	43.07	0.01627	78.20654	28
Model C-75-135	71.50	7040.84	43.43	0.01625	78.14297	27
Model C-105-135	80.09	7042.36	38.73	0.01524	73.28239	39
Model D-15	50.15	7076.97	62.85	0.02036	97.86286	4
Model D-45	55.90	7047.25	57.92	0.01903	91.51011	9
Model D-75	66.47	7038.31	48.67	0.01708	82.13399	21
Model D-105	77.55	7040.59	40.74	0.01556	74.81248	35
Model D-135	86.43	7045.29	36.66	0.01468	70.55413	51
Model D-15-45	**47.95**	**7077.70**	**62.85**	**0.02080**	**100**	**1**
Model D-15-75	50.57	7078.45	60.09	0.02011	96.67327	5
Model D-15-105	50.30	7077.95	64.65	0.02044	98.26543	2
Model D-15-135	50.22	7077.60	64.24	0.02043	98.21463	3
Model D-45-75	53.14	7046.34	59.82	0.01960	94.22218	6
Model D-45-105	55.00	7047.54	57.41	0.01915	92.04424	8
Model D-45-135	55.55	7047.47	59.65	0.01920	92.28292	7
Model D-75-105	64.21	7036.72	50.53	0.01745	83.90252	15
Model D-75-135	64.99	7037.64	49.06	0.01727	83.03961	20
Model D-105-135	75.83	7038.83	43.66	0.01588	76.34625	34

4 Crashworthiness performance optimization method based on machine learning

4.1 Design of experiments

Apart from the number and position of initiators, the crashworthiness performance of a square tube strongly relies on the size of the initiators. Thus, a machine learning optimization method was adopted herein to seek improved crush performance. The optimal Latin hypercube sampling (Opt LHS) could be employed to effectively generate the sample points in a crashworthiness performance study [43, 44]. The Opt LHS method was thus utilized to generate 150 sample points considering variations in the selected design variables based on the previous research and experience [22].

4.2 Prediction and machine learning model selection

In this study, the FE simulation results were randomly split into 90% training and 10% validation sets. KNN, SVM, and RF, were employed to predict the square tube crashworthiness responses. Every model was evaluated with 10-fold cross-validation, while the grid search was used to find the optimum super parameters.

4.2.1 Prediction for IPF, EA, and CFE

The observed and predicted value of IPF, EA and CFE are graphed in Fig. 9 (a), (b), and (c), respectively. In the IPF prediction situation, the largest R^2 (0.99) obtained from the SVM model is 5.32% and 1.02% larger than that of KNN (0.94) and RF (0.98), respectively. Besides, the SVM model presented the highest R^2 (0.99), which is 33.78% and 20.73% larger than that of KNN (0.74) and RF (0.82), respectively, in the EA prediction situation. Furthermore, the largest R^2 (0.981) observed from the SVM model in the CFE situation is 6.47% and 0.25% larger than that of KNN (0.921) and RF (0.979), respectively. Clearly, the results highlight that the SVM had the best accuracies.

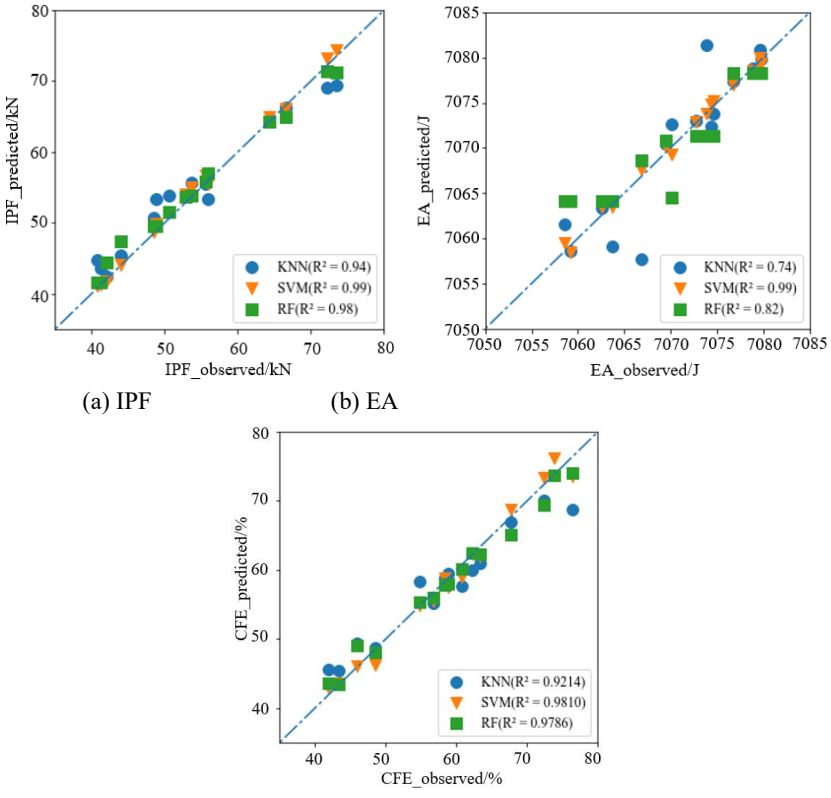

(a) IPF (b) EA

(c) CFE

Fig. 9 Performance of machine learning models on (a) IPF; (b) EA; (c) CFE.

4.2.2 Prediction for deformation mode

The square tubes with rectangular-type crush initiators presented two deformation modes, namely complete and non-complete modes, were labeled as 0 and 1, respectively. In the complete deformation mode, there is no uncompressed position in

the square tube, while there is an uncompressed position in the square tube in the non-complete deformation mode. Thus, the non-complete section deformation mode should be eliminated since the numerical operation cannot deal with this deformation mode, which is a categorical response. As depicted in Fig 10, the deformation mode was also predicted using KNN, SVM, and RF machine learning techniques.

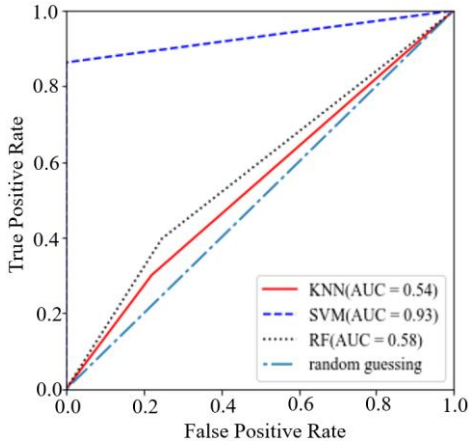

Fig. 10 ROC curves for deformation mode obtained from machine learning models.

Besides, the receiver operating characteristic (ROC) curve was used to evaluate the prediction models. The area under the curve (AUC) was employed to mathematically calculate the ROC curve area to demonstrate the classification model's performance. The value of AUC lies between 0.5 and 1. Moreover, when the AUC of the predictive model is equal to 1, it means that the model is ideal. Fig 15 evidenced that the highest AUC (0.93) which was obtained from the SVM model is 72.22% and 60.34% higher than that of KNN (0.54) and RF (0.58), respectively, indicating that the SVM model had the highest accuracy and could be reliable in predicting deformation mode.

4.3 Parametric analysis

~~A parametric analysis is presented herein based on the FE simulation results to represent the distribution of responses and the influences of variables. Fig. 14, 15, and 16 graphed the deformation, IPF, EA, and CFE distribution for variables of initiators, respectively.~~

Fig. 11 presents the deformation distribution. When analyzing the influence of two parameters, the other two parameters were fixed as their own lower and higher values, respectively. A noticeable change trend is that the deformation transferred from non-

complete deformation mode to complete deformation mode with increasing *b* and *c* (*geometry linked to Figure 7*).

However, the effect of *a* and *d* on the deformation mode depends on the other two parameters. On the one hand, when *c* is at a small value, the deformation changes from non-complete deformation mode to complete deformation mode as *a* increases. On the other hand, when *c* is at a higher value, the deformation changes from complete deformation mode to non-complete deformation mode as *a* increases. And under the condition that *a* is lower, as *b* increases, the deformation changes from complete deformation mode to non-complete deformation mode.

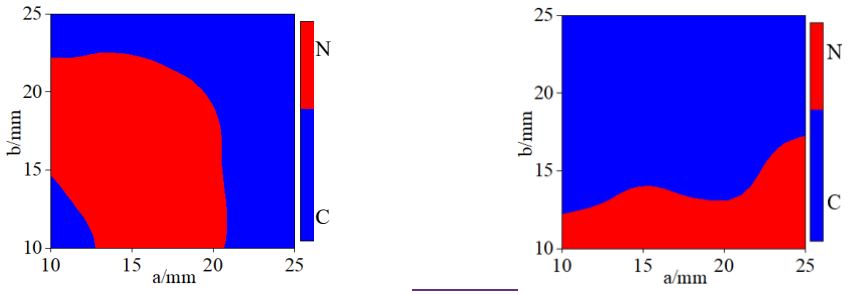

(a) c = lower, d = lower

(b) c = higher, d = lower

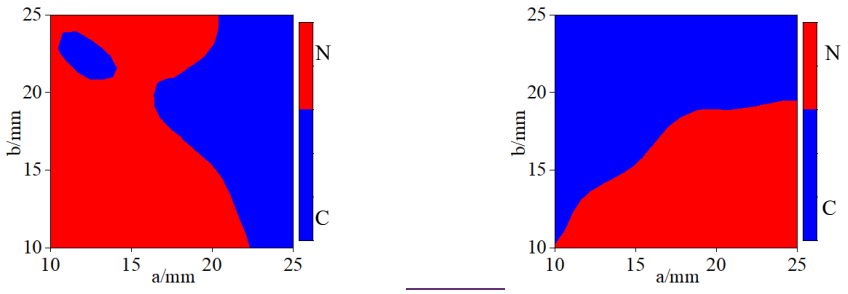

(c) c = lower, d = higher

(d) c = higher, d = higher

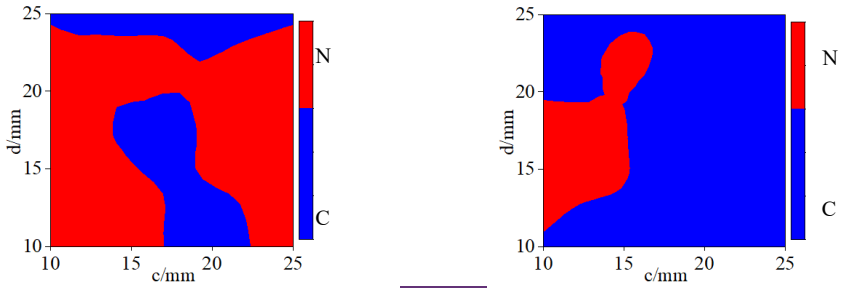

(e) a = lower, b = lower

(f) a = lower, b = higher

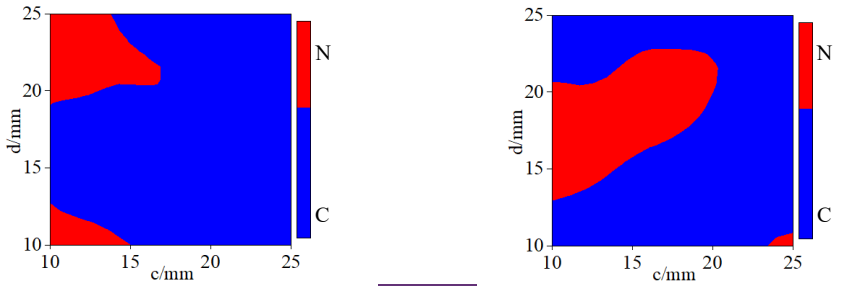

(g) a = higher, b = lower (h) a = higher, b = higher

Fig. 11 Deformation mode with different initiator parameters (N, non-complete deformation mode, graphed in red; C, complete deformation mode, graphed in blue).

4.3.2 Parametric analysis on IPF, EA, and CFE

The IPF, EA and CFE distribution with different geometric parameters were illustrated in Fig. 12, 13, and 14 respectively. The results showed that the nonlinearity of EA and CFE was obviously significantly greater than that of IPF. In addition, the results indicated that the linearity of IPF was significantly stronger than those of EA and CFE, while the change trends of the three responses were essentially identical; that is, all three responses increased with increasing *a* but slightly decreased when *b* increased. Besides, the IPF and EA increased with decreasing *c* when a reaches its lower limits. However, there is no clear trend for the effect of d on IPF, EA, and CFE. Combined with the deformation mode distribution, it can be found that when the deformation mode was non-complete deformation mode, the effect of *b* and *c* on the three crashworthiness responses were more significant than that of *a* and *d*.

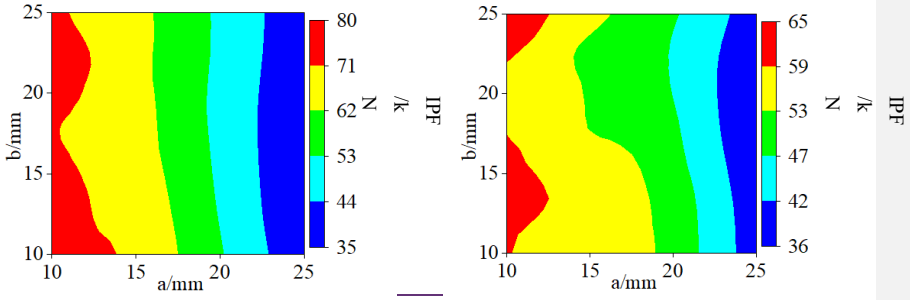

(a) c = lower, d = lower (b) c = higher, d = lower

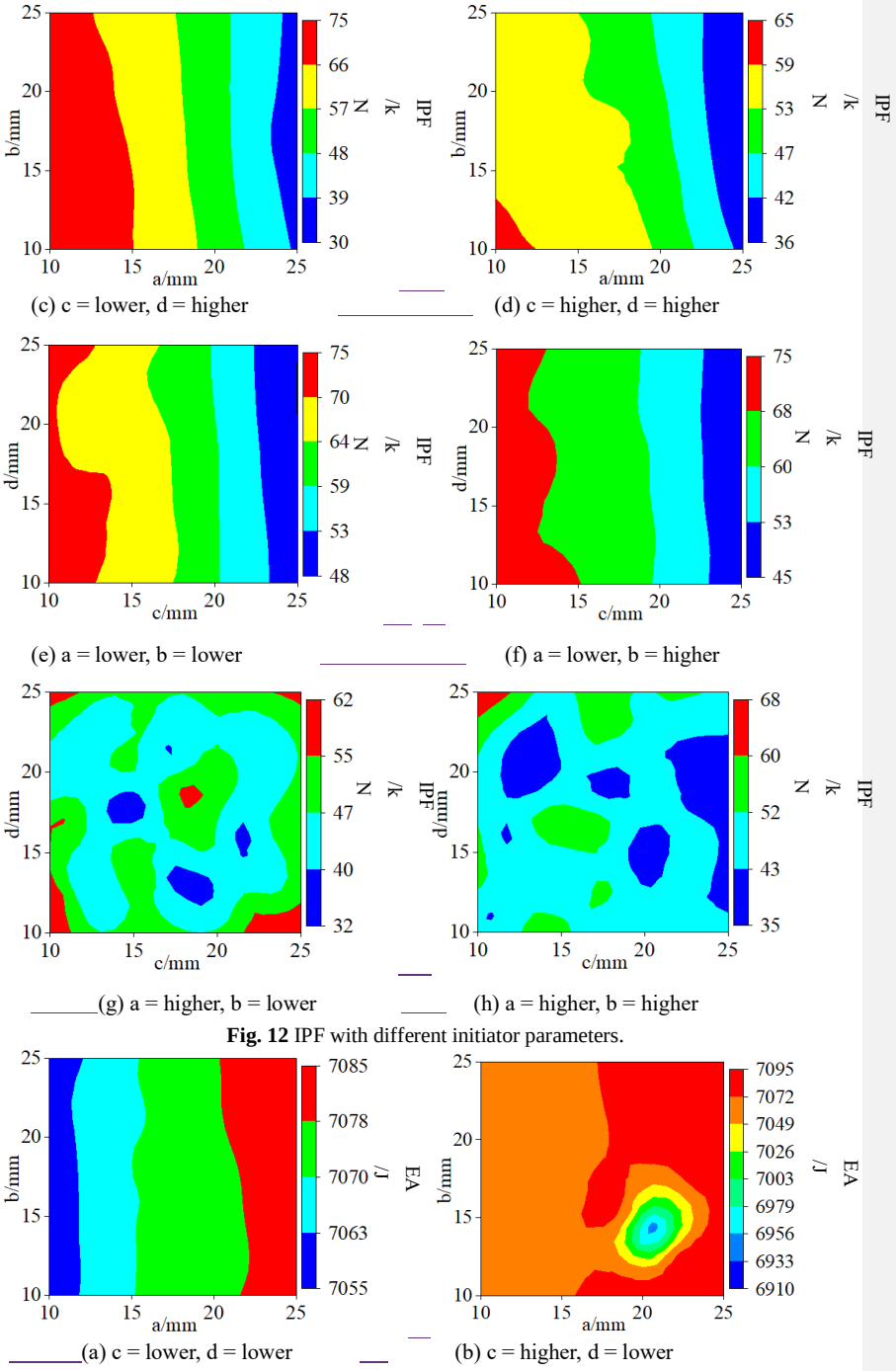

Fig. 12 IPF with different initiator parameters.

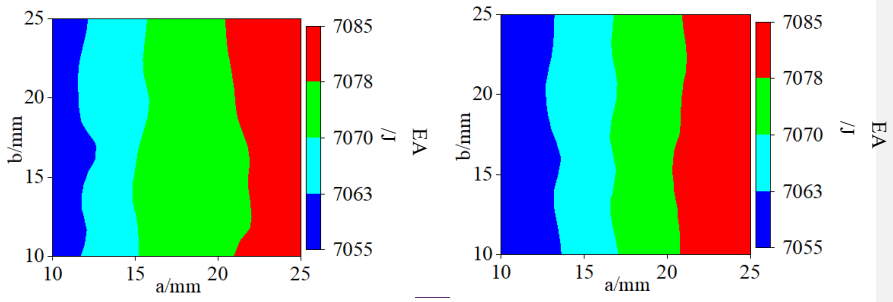

(c) c = lower, d = higher

(d) c = higher, d = higher

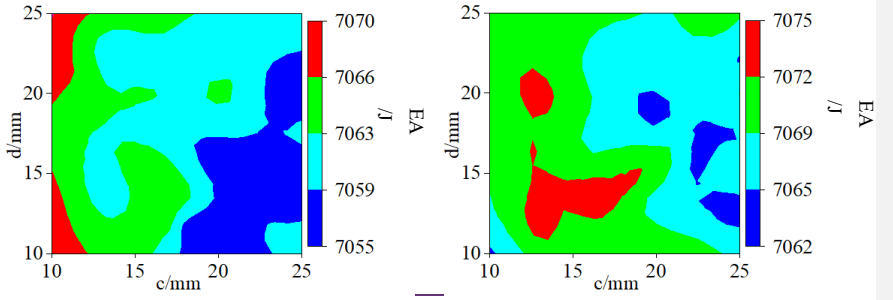

(e) a = lower, b = lower

(f) a = lower, b = higher

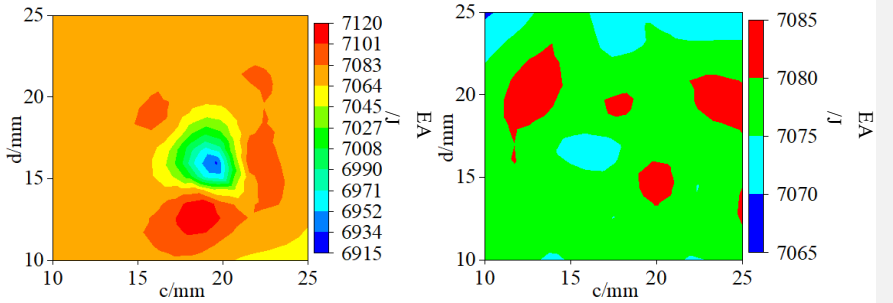

(g) a = higher, b = lower

(h) a = higher, b = higher

Fig. 13EA with different initiator parameters.

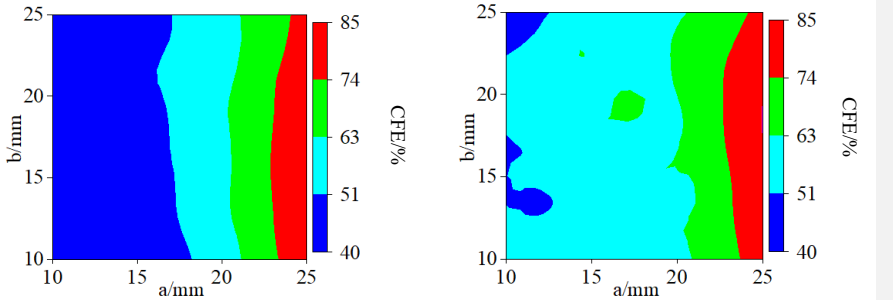

(a) c = lower, d = lower

(b) c = higher, d = lower

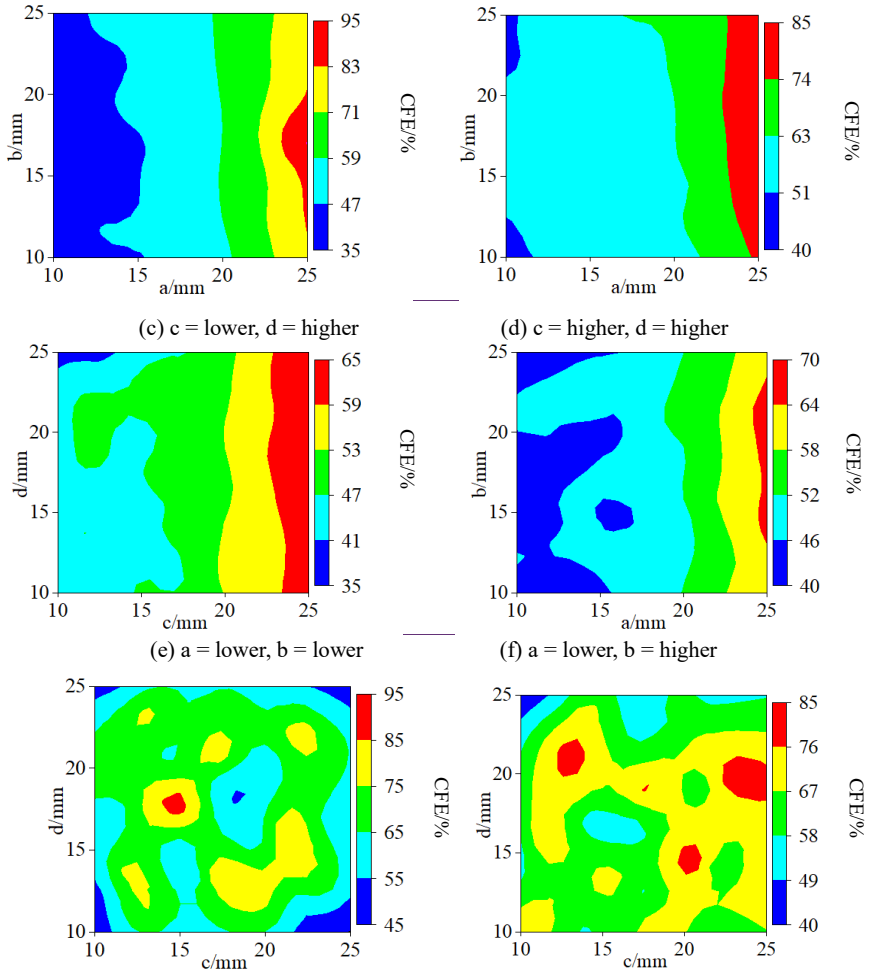

Fig. 14 CFE with different initiator parameters.

5 Optimization with SVM

5 .1 Optimization processes

A multi-objective crashworthiness optimization was prescribed to demonstrate the efficacy of the proposed machine learning-based optimization method and to identify the optimal square tube with the lowest IPF and the highest EA and CFE. In addition, the round function is used to restrict width and height values to one decimal place when determining the optimal value, as demonstrated by the equations in Eqs (15).

$$\begin{cases} \text{Min(IPF, -EA, -CFE)} \\ s.t. \begin{cases} \textit{deformation mode} = 0 \\ 10mm \le \text{a}, b \le 25mm \\ \text{Roud(a,1)} \\ \text{Roud}(b,1) \\ \text{Roud}(c,1) \\ \text{Roud}(d,1) \end{cases} \end{cases} \quad (15)$$

Where a and b are the height and width size of the first initiator alone axial direction, respectively, and c and d are the height and width size of the second initiator alone axial direction, respectively.

NSGA-II, a multi-objective optimization algorithm, was employed to find the optimum geometric configuration with minimum IPF, maximum EA, and CFE. The maximum number of generations was set to 1000, and the population size that constraints the Pareto front solution points was set to 50 [22].

5.2 Results and discussion

The optimal design parameters and crashworthiness response are presented in Table 5. In the Pareto set, the width of the first initiator along the axial direction (a) showed a trend of being smaller than the width of the second initiator along the axial direction initiator (c). In contrast, twenty over fifty of the width of the first initiator (b) showed a trend of being basically the same as or smaller than the width of the second initiator (d). Besides, the higher of a reaches 25 mm, while the lower limit of b, c, and d is close to 10 mm. Furthermore, the most area of the first initiator ($a \times b$) is larger than that of the second initiator ($c \times d$), indicating that a larger first initiator than the second was considered to perform a complete deformation mode with a minimum IPF and maximum EA and CFE.

In addition, after obtaining the optimized height and width values from the SVM, the lower limit of IPF (33.94 kN), EA (7081.71J), and CFE (80.34%) obtained from the Pareto fronts is -29.22%, 0.06%, 27.83% higher than those (IPF: 47.95 kN, EA: 7077.70J; CFE: 62.85 %) of the best choice observed form COPRAS, respectively. Furthermore, the upper limit of IPF (37.43 kN), EA (7083.51 J), and CFE (85.90 %) obtained from the Pareto fronts are -21.94%, 0.08%, 36.67% higher than those of the

best choice obtained from the COPRAS, respectively, as showed in Table 6.

Moreover, the deformation modes of the samples in the Pareto front were graphed in Table 7. The results demonstrated that the optimized solutions prescribed complete mode, indicating that the proposed machine learning based optimization method can effectively remove the undesirable deformation modes in the multi-objective optimization of the square tubes with initiators.

Table 5 Pareto set of the square tube

No.	a/mm	b/mm	c/mm	d/mm	IPF/kN	EA/J	CFE/%
1	25.0	13.4	10.0	10.0	35.74	7081.81	85.85
2	25.0	25.0	25.0	25.0	33.94	7082.79	81.97
3	25.0	18.8	18.2	25.0	37.33	7083.51	80.49
4	25.0	25.0	19.6	25.0	36.01	7083.22	79.99
5	25.0	14.7	10.0	10.0	35.74	7081.95	85.90
6	25.0	17.5	14.4	24.1	37.38	7083.31	81.77
7	25.0	18.8	13.0	25.0	36.92	7083.30	82.26
8	25.0	20.3	21.9	19.7	36.39	7083.08	81.82
9	25.0	25.0	25.0	21.7	34.12	7082.63	82.68
10	25.0	19.7	24.7	18.7	35.39	7082.84	83.00
11	25.0	21.7	25.0	25.0	34.70	7083.05	82.01
12	25.0	20.0	24.7	25.0	35.25	7083.16	81.66
13	25.0	25.0	25.0	18.7	34.25	7082.52	83.18
14	25.0	25.0	25.0	11.8	34.47	7082.39	83.60
15	25.0	17.7	10.0	10.3	35.78	7082.23	85.62
16	25.0	24.4	25.0	11.0	34.56	7082.43	83.68
17	25.0	20.8	24.7	20.8	35.15	7082.90	82.76
18	25.0	19.2	10.0	10.1	35.80	7082.31	85.27
19	25.0	20.7	25.0	22.4	35.00	7082.95	82.56
20	25.0	18.8	14.4	25.0	37.19	7083.40	81.59
21	25.0	18.8	23.1	25.0	36.22	7083.33	80.86
22	25.0	20.0	24.7	22.3	35.30	7083.00	82.34
23	25.0	21.6	24.7	16.2	35.06	7082.69	83.50
24	25.0	23.2	10.0	23.8	35.58	7082.92	83.07
25	25.0	17.2	10.0	24.7	36.11	7082.92	84.41
26	25.0	18.8	10.0	24.7	35.95	7082.98	84.20
27	25.0	21.2	20.4	25.0	36.54	7083.42	80.53
28	25.0	22.6	20.4	25.0	36.27	7083.36	80.47
29	25.0	22.6	10.0	10.0	35.87	7082.41	84.00
30	25.0	17.7	10.0	20.4	36.04	7082.65	85.00
31	25.0	22.6	14.4	25.0	36.67	7083.35	81.04
32	25.0	22.1	14.4	25.0	36.73	7083.37	81.16
33	25.0	22.5	24.7	20.8	34.81	7082.82	82.84
34	25.0	18.8	11.8	25.0	36.60	7083.20	82.95
35	25.0	21.7	25.0	12.5	34.90	7082.58	83.87
36	25.0	13.7	10.0	10.0	35.74	7081.84	85.87
37	25.0	15.4	10.0	10.0	35.75	7082.03	85.88
38	25.0	17.2	10.0	22.0	36.10	7082.72	84.84
39	25.0	16.1	10.0	15.1	35.99	7082.26	85.70
40	25.0	19.5	10.0	14.6	35.90	7082.44	85.13
41	25.0	20.0	15.0	25.0	37.10	7083.43	81.27
42	25.0	21.7	25.0	10.8	34.89	7082.56	83.85

43	25.0	21.2	16.7	25.0	36.99	7083.47	80.68
44	25.0	15.4	10.0	24.1	36.29	7082.77	84.59
45	25.0	21.7	25.0	19.1	34.85	7082.76	83.30
46	25.0	21.7	10.1	25.0	35.70	7083.04	83.39
47	25.0	18.8	15.5	25.0	37.32	7083.45	81.16
48	25.0	19.2	10.0	20.7	35.94	7082.72	84.69
49	25.0	20.3	21.9	25.0	36.30	7083.38	80.75
50	25.0	18.8	24.5	25.0	35.64	7083.22	81.34

Table 6 Optimal design parameters and results

	IPF/kN	EA/J	CFE/%	Deformation mode
The best choice observed from COPRAS	47.95	7077.70	62.85	1
The lower limit of the Pareto front	33.94	7081.71	80.34	0
The upper limit of the Pareto front	37.43	7083.51	85.90	0

Table 7 Deformation modes observed from the Pareto front of the square tubes.

1	2	3	4	5
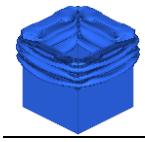	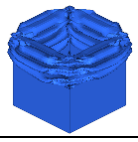	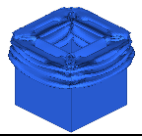	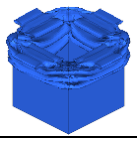	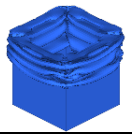
6	7	8	9	10
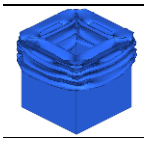	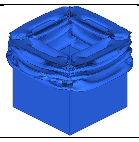	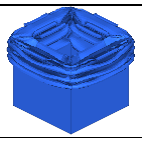	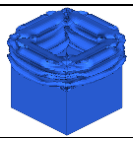	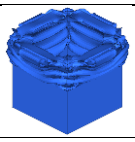
11	12	13	14	15
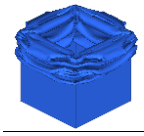	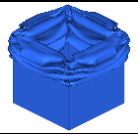	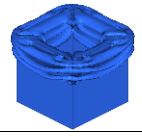	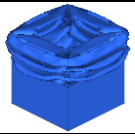	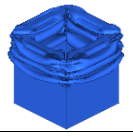
16	17	18	19	20
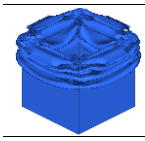	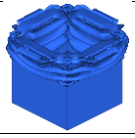	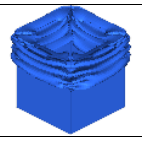	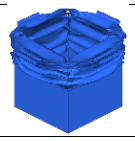	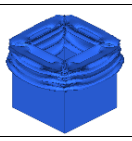
21	22	23	24	25
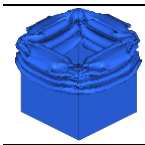	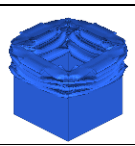	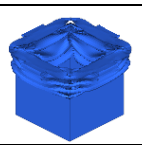	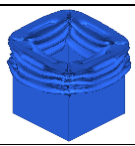	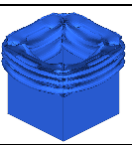
26	27	28	29	30
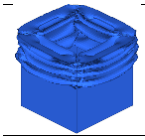	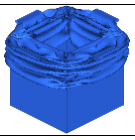	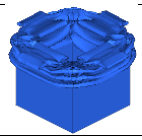	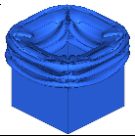	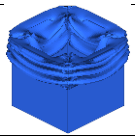
31	32	33	34	35

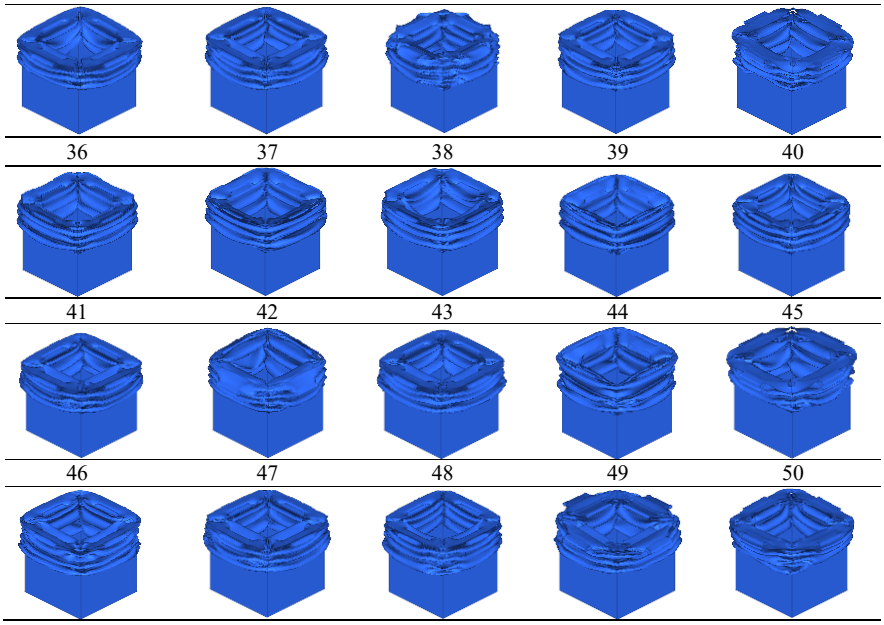

6 Conclusion

This study proposed a machine learning based optimization method to remove the undesired deformation mode and investigate the influence of the initiator's size on the crashworthiness performance. Within its limitation of the study, some more specific conclusions can be drawn as follows:

(1) All the number, position, and size of the initiators significantly affected square tubes' crashworthiness behaviors.

(2) The square tube with two sets of four corner holes along the axial direction was the most competent of all these specimens.

(3) A larger area of the first initiator than that of the second was expected to perform better crashworthiness.

(4) The proposed machine learning-based optimization method was reasonably effective in predicting and optimizing the square tube's crashworthiness.

Acknowledgments

This paper is supported by the National Natural Science Foundation of China (Grant No. 51605353) and Scientific Research Funds of Guilin University of Aerospace Technology (Grant No. XJ20KT15).

Reference

[1] Yin H, Xiao Y, Wen G, Qing Q, Deng Y. Multiobjective optimization for foam-filled multi-cell thin-walled structures under lateral impact. Thin-Walled Structures. 2015;94:1-12.

[2] I. EREN YG, Z. AKSOY. Finite element analysis of collapse of front side rails with new types of crush initiators. International Journal of Automotive Technology. 2009;10:451−7.

[3] Arnold B AW. Experimental observations on the crush characteristics of AA6061 T4 and T6 structural square tubes with and without circular discontinuities. International Journal of Crashworthiness. 2004;9:73-87.

[4] Jiang H, Ren Y, Gao B, Xiang J, Yuan F-G. Design of novel plug-type triggers for composite square tubes: enhancement of energy-absorption capacity and inducing failure mechanisms. International Journal of Mechanical Sciences. 2017;131-132:113-36.

[5] Yamaguchi S KH, Okazaki T. Efficient energy absorption of automobile side rails. SAE. 1985.

[6] AA Singace E-SH. Behaviour of axially crushed corrugated tubes. International Journal of Mechanical Sciences. 1997;39:249-68.

[7] Siromani D, Henderson G, Mikita D, Mirarchi K, Park R, Smolko J, et al. An experimental study on the effect of failure trigger mechanisms on the energy absorption capability of CFRP tubes under axial compression. Composites Part A: Applied Science and Manufacturing. 2014;64:25-35.

[8] DiPaolo BP, Monteiro PJM, Gronsky R. Quasi-static axial crush response of a thin-wall, stainless steel box component. International Journal of Solids and Structures. 2004;41:3707-33.

[9] Sastranegara A, Adachi T, Yamaji A. Improvement of energy absorption of impacted column due to transverse impact. International Journal of Impact Engineering. 2005;31:483-96.

[10] Cheng Q, Altenhof W, Li L. Experimental investigations on the crush behaviour of AA6061-T6 aluminum square tubes with different types of through-hole discontinuities.

Thin-Walled Structures. 2006;44:441-54.

[11] Gümrük R, Karadeniz S. A numerical study of the influence of bump type triggers on the axial crushing of top hat thin-walled sections. Thin-Walled Structures. 2008;46:1094-106.

[12] Mamalis AG, Manolakos DE, Spentzas KN, Ioannidis MB, Koutroubakis S, Kostazos PK. The effect of the implementation of circular holes as crush initiators to the crushing characteristics of mild steel square tubes: experimental and numerical simulation. International Journal of Crashworthiness. 2009;14:489-501.

[13] Cho Y-B, Bae C-H, Suh M-W, Sin H-C. A vehicle front frame crash design optimization using hole-type and dent-type crush initiator. Thin-Walled Structures. 2006;44:415-28.

[14] Gupta N K GSK. Effect of annealing, size and cut-outs on axial collapse behaviour of circular tubes. International Journal of Mechanical Sciences. 1993;35:597-613.

[15] Tarlochan F, Samer F, Hamouda AMS, Ramesh S, Khalid K. Design of thin wall structures for energy absorption applications: Enhancement of crashworthiness due to axial and oblique impact forces. Thin-Walled Structures. 2013;71:7-17.

[16] Alavi Nia A, Fallah Nejad K, Badnava H, Farhoudi HR. Effects of buckling initiators on mechanical behavior of thin-walled square tubes subjected to oblique loading. Thin-Walled Structures. 2012;59:87-96.

[17] Han H, Taheri F, Pegg N. Quasi-static and dynamic crushing behaviors of aluminum and steel tubes with a cutout. Thin-Walled Structures. 2007;45:283-300.

[18] Bodlani SB, Yuen SCK, Nurick GN. The Energy Absorption Characteristics of Square Mild Steel Tubes With Multiple Induced Circular Hole Discontinuities—Part II: Numerical Simulations. Journal of Applied Mechanics. 2009;76.

[19] Zhu F, Logakannan K. Crash Safety Design for Lithium-ion Vehicle Battery Module with Machine Learning. SAE2022.

[20] Kazi M-K, Eljack F, Mahdi E. Design of composite rectangular tubes for optimum crashworthiness performance via experimental and ANN techniques. Composite Structures. 2022;279.

[21] Kohar CP, Greve L, Eller TK, Connolly DS, Inal K. A machine learning framework

for accelerating the design process using CAE simulations: An application to finite element analysis in structural crashworthiness. Computer Methods in Applied Mechanics and Engineering. 2021;385:114008.

[22] Li Z, Ma W, Yao S, Xu P, Hou L, Deng G. A machine learning based optimization method towards removing undesired deformation of energy-absorbing structures. Structural and Multidisciplinary Optimization. 2021.

[23] Harrinton P. Machine learning in action: Manning Publications Co, 2012.

[24] Flach PA. Machine Learning - The Art and Science of Algorithms that Make Sense of Data. 2012.

[25] Li Z, Rakheja S, Shangguan W-B. Study on crushing behaviors of foam-filled thin-walled square tubes with different types and number of initiators under multiple angle loads. Thin-Walled Structures. 2019;145.

[26] Lan Goodfellow YB, Aaraon Courville. Deep learning. Massachusetts: MIT Press, 2017.

[27] Tin Kam H. Random decision forests. Proceedings of 3rd International Conference on Document Analysis and Recognition1995. p. 278-82 vol.1.

[28] Wiener ALM. Classification and Regression by randomForest. R News. 2002;2/3:18-22.

[29] Langseth M, Hopperstad OS, Hanssen AG. Crash behaviour of thin-walled aluminium members. Thin-Walled Structures. 1998;32:127-50.

[30] Reyes A, Hopperstad OS, Hanssen AG, Langseth M. Modeling of material failure in foam-based components. International Journal of Impact Engineering. 2004;30:805-34.

[31] Liang R, Liu X, Hu Y, Jiang C, Bastien C. A methodology to investigate and optimise the crashworthiness response of foam-filled twelve right angles thin-walled structures under axial impact. Composite Structures. 2023:116736.

[32] Yin H, Wen G, Liu Z, Qing Q. Crashworthiness optimization design for foam-filled multi-cell thin-walled structures. Thin-Walled Structures. 2014;75:8-17.

[33] Zhang Z, Liu S, Tang Z. Comparisons of honeycomb sandwich and foam-filled cylindrical columns under axial crushing loads. Thin-Walled Structures. 2011;49:1071-

9.

[34] WHO. Road Traffic Injuries. World Health Organization. 2020 ed2020.

[35] RAGLAND CL, FESSAHAIE O, ELLIOTT D. Evaluation of frontal offset/oblique crash test conditions. PROCEEDINGS OF 17TH INTERNATIONAL TECHNICAL CONFERENCE ON THE ENHANCED SAFETY OF VEHICLES CD ROM. Amsterdam , Netherlands2001.

[36] Pirmohammad S, Marzdashti SE. Crushing behavior of new designed multi-cell members subjected to axial and oblique quasi-static loads. Thin-Walled Structures. 2016;108:291-304.

[37] Zhang S, Xu F. A two-stage hybrid optimization for honeycomb-type cellular structures under out-of-plane dynamic impact. Applied Mathematical Modelling. 2020;80:755-70.

[38] Hanssen AG, Langseth M, Hopperstad OS. Static crushing of square aluminium extrusions with aluminium foam filler. International Journal of Mechanical Sciences. 1999;41:967-93.

[39] Chatterjee P, Chakraborty S. Material selection using preferential ranking methods. Materials & Design. 2012;35:384-93.

[40] Chatterjee P, Athawale VM, Chakraborty S. Materials selection using complex proportional assessment and evaluation of mixed data methods. Materials & Design. 2011;32:851-60.

[41] Zavadskas EK, Turskis Z, Tamošaitiene J, Marina V. Multicriteria selection of project managers by applying grey criteria. Ukio Technologinis ir Ekonominis Vystymas. 2008;14:462-77.

[42] Sun G, Liu T, Huang X, Zheng G, Li Q. Topological configuration analysis and design for foam filled multi-cell tubes. Engineering Structures. 2018;155:235-50.

[43] Liu X, Liang R, Hu Y, Tang X, Bastien C, Zhang R. Collaborative optimization of vehicle crashworthiness under frontal impacts based on displacement oriented structure. International Journal of Automotive Technology. 2021;22:1319–35.

[44] Liao X, Li Q, Yang X, Zhang W, Li W. Multiobjective optimization for crash safety design of vehicles using stepwise regression model. Structural and Multidisciplinary

Optimization. 2007;35:561-9.